Chapter 11

Analysis and Application of Decaying Turbulence with Initial Fractal Geometry

Hiroki Suzuki, Shinsuke Mochizuki,
Yasuhiko Sakai and Koji Nagata

Additional information is available at the end of the chapter

http://dx.doi.org/10.5772/67942

Abstract

In this paper, we address high-Schmidt-number (Sc) scalar turbulent mixing that results from grid-generated turbulence using the initial fractal geometry of the velocity profile. More specifically, as was proposed in our recent study, we adopt an initial flow field generated by a fractal grid and apply it to a water channel experiment based on a high-Sc-number scalar-mixing layer in order to create grid-generated turbulence, and thus solve our current research problem. The high-Sc-number scalar and velocity fields of the grid-generated turbulence are then measured using planar laser-induced fluorescence (PLIF) and particle image velocimetry (PIV), respectively. By means of fractal analysis, this study specifically addresses the turbulent mixing phenomena in which the fractal dimension of the mixing interface of an observed high-Sc-number scalar field is calculated. Additionally, we discuss the efficiency of using fractal grids as devices for enhancing high-Sc-number scalar turbulent mixing by observing turbulent intensities and dissipation by PIV.

Keywords: fractal analysis, fractal dimension, turbulent mixing, grid-generated turbulence, initial value problem

1. Introduction

Fractals are widely found in nature. In fluid mechanics, the fractals found in turbulence have been investigated as a means of understanding and modeling fundamental phenomena, one of which is the non-Gaussian nature found in small-scale fluctuations [1]. For instance, since the skewness factor of a longitudinal velocity derivative that relates to turbulence vortex stretching is approximately −1 to −0.2 rather than zero, small-scale turbulence fields, in which

the probability density distribution of fluctuations is described by a non-Gaussian function, have been discussed from the perspective of fractals. In such turbulent flows, kinetic energy is first injected into a large-scale region, after which it is transferred to a smaller-scale region, before dissipating into the smallest-scale region. In such cases, it is possible to formulate the transfer of kinetic energy in the inertial subrange. For structure function modeling, which also characterizes the nature of turbulent flows in physical space, the fractal perspective, in which the fractal dimension is a characteristic quantity, is applied [2]. In engineering applications, turbulent flows are often considered to be mixers, and the flows produced are thus referred to as turbulent mixing [3]. The characteristics of the mixing interface between two mixtures, which increases in area with time due to turbulent mixing, can also be quantified by using the fractal method.

Turbulence decays temporally when the mean flow does not provide kinetic energy to the turbulence. In decaying turbulence, kinetic energy follows the decay law (the parameters of which are the decay coefficient and decay exponent) and has been examined in previous studies (e.g., [4–6]). The decay coefficient magnitude relates to the drag coefficient of a turbulence-generating grid, while the decay exponent magnitude is of the order of unity and could be used to characterize the decay characteristics of decaying homogeneous turbulence. Recent studies (e.g., [7, 8]) have examined the effects of the initial conditions on the turbulence decay characteristics. Specifically, it has been determined that, within the range of moderate Reynolds numbers, decay exponent values depend on the initial turbulence decay conditions. Additionally, since the initial fractal geometry of the velocity profile may affect grid-generated turbulence decay characteristics, thereby resulting in turbulence decay, the effects of the initial velocity profile fractal geometry on decaying turbulence have also been investigated in several previous studies (e.g., [9–23]). These studies investigated turbulence produced by a fractal geometry turbulence-generating grid (referred to hereafter as a fractal grid (FG)) and most such studies used turbulence created by a square-type fractal grid (referred to hereafter as fractal grid turbulence) when conducting wind tunnel experiments (e.g., [10–14]), water channel experiments (e.g., [15–17]), and numerical simulations (e.g., [18–23]).

Since the observed diffusion resulting from turbulence has been determined to be much larger than that which can be produced by viscous diffusion, one of the engineering applications of turbulence is turbulent mixing. In addition, since rapid turbulence mixing of heat and mass due to turbulence has obvious engineering applications, there have been previous studies that have attempted to enhance such mixing (e.g., [24, 25]). However, few works have applied water channel experiments to the study of high-Schmidt-number (Sc) scalar mixing caused by fractal grid turbulence [26]. Since the diffusion coefficient of a high-Sc-number scalar is significantly smaller than that of heat in air and water, the contribution of turbulent diffusion is dominant in high-Sc-number scalar turbulent mixing. Therefore, this study will address turbulent mixing by focusing on the fractal geometry of the initial velocity profile, which is set using a fractal grid. More specifically, high-Sc-number scalar turbulent mixing resulting from turbulent diffusion in fractal grid turbulence will be examined, and mixing interfaces will be discussed in terms of fractals to clarify the effects of turbulent mixing resulting from fractal grid turbulence.

http://dx.doi.org/10.5772/67942

In this section, the effects of the initial fractal geometry of the velocity profile on the turbulent mixing characteristics, and the high-Sc-number scalar-mixing layer in grid-generated turbulence, are presented. As in our previous study, a flow with an initial fractal geometry is generated using a fractal grid, but the present experiment is based on a water channel experiment and utilizes both planar laser-induced fluorescence (PLIF) (e.g., [27, 28]) and particle image velocimetry (PIV) (e.g., [29]) to investigate the high-Sc and fluctuating velocity fields. Note that the PLIF and PIV apparatuses used herein were constructed in-house and are validated in the present work.

The fractal dimensions of the mixing interface (e.g., [30, 31]) as well as the turbulent statistics in the high-Sc-number scalar-mixing layer, where the fractal dimension is calculated using the box counting method, are shown. Additionally, we discuss the efficiency of fractal grids as devices for enhancing turbulent mixing by using the turbulent intensities and viscous dissipations measured via PIV, and then show a periodic box approach to further address the effects of the initial fractal geometry of the velocity profile on the decay characteristics and turbulent mixing. The Fourier spectral method used for the periodic box approach simulations is also described and verified.

2. Experimental analysis

2.1. Flow and mass transfer fields

In this section, we discuss flow and mass transfer fields in regular grid and fractal grid turbulences. **Figure 1** shows schematic diagrams of the experimental apparatus used. The size of the test section in the present water channel experiment is 1500 × 100 × 100 [mm^3] for the streamwise (x), transverse (y), and span-wise (z) directions, respectively. The coordinate system origin is set at the center of the turbulence-generating grid. A head tank is used to provide the free stream, and a splitter plate is placed in the contraction upstream of the test section to produce the scalar-mixing layer.

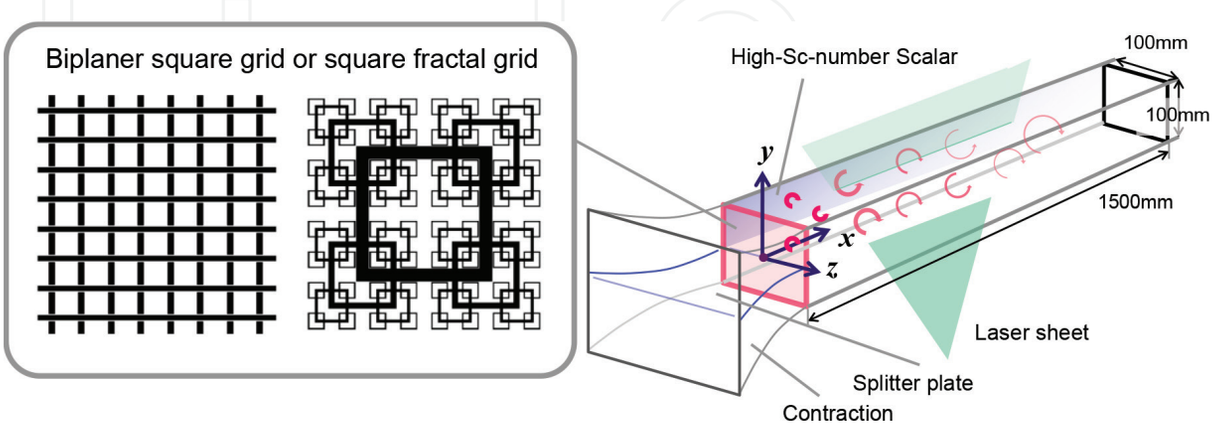

Figure 1. Water-channel experiment schematics. The origin of the coordinate system is placed at the center of the turbulence-generating grid. In this experiment, a biplane square grid or a square fractal grid is set at the entrance of the test section.

An aqueous solution of Rhodamine B, which is considered to be a high-Sc-number scalar, is set in the lower layer of the flow leading into the test section. Here, the flow of the upper layer does not include fluorescent dye because the concentration field of a high-Sc-number scalar is measured via the PLIF technique. Since PIV is used to measure the grid-generated turbulence flow field in this experiment, the laser system and high-speed camera used for PLIF and PIV observations were also employed in the present experimental apparatus.

The present study used both square grids and a fractal grid [10] for turbulence generation. In the first experiment, two square grids were used to produce grid-generated turbulence. The first square grid (SG1), which generates conventional grid turbulence (CGT) and was used to validate the PIV and PLIF experiments, consisted of round bars and was the same one used in our previous water-channel experiment [2, 4]. The second square grid (SG2) also generates conventional grid turbulence of which the characteristics were compared with those of fractal grid turbulence. The present fractal grid was based on that proposed by that used in the wind tunnel experiment conducted in the previous studies.

The fractal dimensions D_f of all grids were set at two. The thickness ratio t_r, which is defined as the ratio of thickness between the largest and smallest bars of the grid [10], was set at 1, 1, and 9.76 for SG1, SG2, and FG1, respectively. The grid mesh size M_{eff} was defined as $M_{eff} = (4D^2/P_M)\ (1 - \sigma)^{1/2}$, where D^2 is the cross-sectional area of the channel, P_M is the fractal perimeter length of the grid [10], and $Re_M = U_o M_{eff}/\nu$ is the mesh Reynolds number, where U_o and ν are the cross-sectionally averaged mean velocity and kinematic viscosity, respectively. The mesh sizes of SG1, SG2, and FG1 are 20, 10, and 5.68 [mm], respectively. The mesh Reynolds number Re is defined as $Re = U_o M_{eff}/\nu$ is 2500 for the three turbulence-generating grids. This Reynolds number value is comparable to those used in our previous experiment [15, 24]. Values of U_o for SG1, SG2, and FG1, which are set by using electromagnetic flow meters, are 0.126, 0.251, and 0.442 [m/s], respectively.

2.2. PLIF technique

In the present experiment, the PLIF technique is used to measure the high-Sc-number scalar field. Here, it should be noted that PLIF does not affect the flow field of grid-generated turbulence, and that the spatial resolution of PLIF is sufficiently accurate for scalar field measurements. Therefore, we are confident that the high-Sc-number scalar field in the grid-generated turbulence could be determined accurately.

Rhodamine B was used in the PLIF experiment because it is considered to be a high-Sc-number scalar. The fluorescent dye contained in this solution is excited by a 532-nm continuous wave (CW) laser with a maximum power of approximately 4 W. The measurement region $L_x \times L_y$ is 50 × 100 [mm^2], where L_x and L_y are the width of the measurement region for x and y directions, respectively. The number of grid points $N_x \times N_y$ is 1800 × 3600, where N_x and N_y are the number of pixel points for the x and y directions, respectively.

In this study, the magnitude of fluorescence in the observed high-Sc-number scalar was measured using a Nikon D700 single-lens reflex (SLR) camera, which was deemed suitable for PLIF due to its large pixel number and high sensitivity. Furthermore, the 36.0 × 23.9 [mm^2]

http://dx.doi.org/10.5772/67942

solid-state image-sensing area of the camera corresponds roughly to the image area of a 35-mm film camera. The camera was equipped with a Nikkor 50 mm F/1.2S lens with an optical filter mounted to cutoff dye fluorescence at wavelengths above 540 nm. The F-stop set was set to 2.0, the ISO sensitivity was set to 400, and the depth of bit in the captured RAW images was set to 14 because those settings were deemed appropriate for our PLIF measurements.

In PLIF experiments, a reference image that is captured with a constant concentration under pre-experiment conditions is often used. However, PLIF experiments contained sources of error that could not be eliminated using a reference image alone [27]. Specifically, the observed fluorescence intensity depends on the experimental conditions, which varies continuously even if the dye concentration is constant because the quantum yield of the dye is a function of time. Additionally, since camera gain also depends on time, the excitation laser intensity may experience temporary fluctuations that affect the observed fluorescence intensity. Furthermore, the intensity of the excitation laser is reduced by the presence of fluorescent dye along the laser path, which may produce spatial variations in the fluorescence intensity even if the dye concentration is spatially constant. Accordingly, in this experiment, a post-processing scheme was used to correct for these sources of error. Specifically, the following processing equations were applied: $\beta I_{j+1} \phi = \beta I_j \phi \exp[\varepsilon C'_{ref} (1 - C_j) dy_j]$ and $V_{j+1}/C_{j+1} = (V_j/C_j) \exp[\varepsilon C'_{ref} (1 - C_j) dy_j]$, where a value in the initial state, $j = 0$, is given as follows: $C_0 = V_0/(\beta I_0 \phi)$. Here, the factors, C, V, β, ϕ, and I, are dye concentration, brightness value, camera gain, quantum yield, and laser intensity for a measured image of fluorescence intensity, respectively, which are normalized by those of the reference image. Also, ε and C'_{ref} are the absorption coefficient and the actual concentration for a reference image. **Figure 2** presents schematic diagrams showing our correction method.

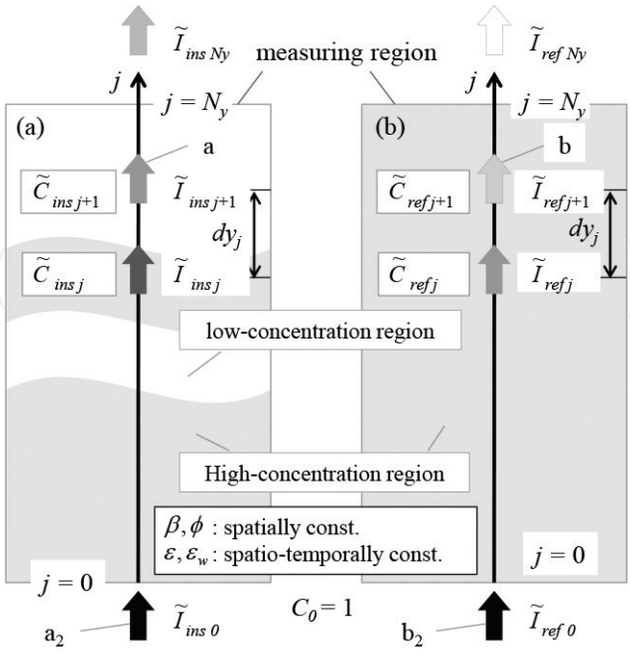

Figure 2. Schematics of observed and reference scalar fields, shown by (a) and (b), used for the present data-processing method in the PLIF. Laser attenuation could also be corrected via the present processing method.

We validated our PLIF technique and examined the effectiveness of the above correction method under the three experimental conditions. In Case 1, the influences of the factors that vary and fluctuate with time and absorption of the excitation laser were reduced; in Case 2, only the influence of the varying factors was reduced; in Case 3, neither the influence of the varying factors nor the laser excitation was reduced. In the validation and examination stage, a scalar-mixing layer in the grid-generated turbulence produced by SG1 was measured. **Figure 3(a)** shows transverse profiles of the mean concentration used for validation and examination. As can be seen in the figure, correcting for factor variations produced a significant influence. By contrast, laser absorption had little effect on the mean concentration profile. The mean concentration profiles of Cases 1 and 2 agree with our previous experiment [24], which used the same experimental conditions as the current experiment. **Figure 3(b)** shows transverse profiles of the variance of concentration fluctuations. As can be seen in the figure, the observed variance of concentration fluctuations is affected by the absorption of the excitation laser as well as the temporally varying/fluctuating factors.

2.3. PIV

In this experiment, PIV was applied to flow field measurements. However, in order to visualize a flow field for measurement, fine polyester particles, the diameter and specific gravity of which were 50 μm and 1.03, respectively, were added to the solution. These particles provided sufficiently high response to flow field fluctuations. In these experiments, particle response to flow field fluctuations was examined using the classical theoretical formula, in which the frequency response and phase lag were calculated. For frequencies up to 1 kHz, the magnitude of both frequency response and phase lag was found to be smaller than 1%. For PIV visualization, we employed the same CW laser that was used in the PLIF experiment, and the high-speed camera was used to capture brightness values for the particles illuminated by the laser. Here, the measurement area $L_x \times L_y$ was 7.5 × 40 [mm^2].

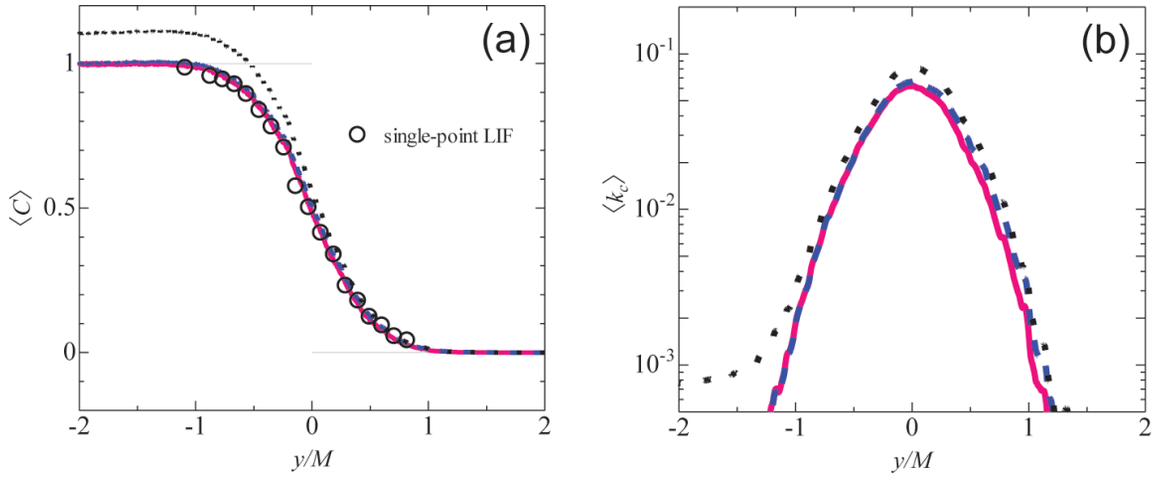

Figure 3. Validation of the present PLIF measurement for mean scalar (a) and scalar fluctuation variance (b). Red-solid, blue-dashed, and black-dotted lines show results of ⟨*C*⟩ and ⟨*kc*⟩ for Cases 1, 2, and 3, respectively. In the mean scalar, the results of Case 3, in which neither the influence of the factors nor laser attenuation is corrected, are shown. In the scalar fluctuation variance results, laser attenuation affects may be significant.

http://dx.doi.org/10.5772/67942

In this experiment, custom-designed software that calculates instantaneous velocity vectors from the set of brightness values for the illuminated fine particles [15] was used. The specific process was as follows. First, the temporal field of brightness value was calculated from the captured images by using Open Source Computer Vision (Open CV), which eliminated the need to conduct preprocedures. The main framework of our PIV is based on the recursive local-correlation method with a 50% overlap. Here, the interrogation windows with the offset determined were applied to the PIV software using the iterative procedure. For subpixel analysis, the gradient method was used instead of Gaussian fitting because the latter requires large interrogation windows to reduce the PIV experimental uncertainty, and because the spatial resolution of the PIV could be improved sufficiently via the gradient method.

We validated our PIV using grid-generated turbulence measurements that were conducted before the PIV measurement results were obtained. The grid-generated turbulence used for the validation of the present PIV was the same as that used for PLIF measurements. **Figure 4(a)** shows the intensity of streamwise velocity fluctuations along the centerline. As shown in the figure, the streamwise profile of the velocity intensity could be approximated by a power law. The agreement of the intensity of the velocity fluctuations with the power law validates the PIV measurement. In the present study, the decay exponent of the power law, where the decay exponent magnitude is on the order of unity, was also measured. As shown in our previous works, decay exponent values can be larger than unity. The decay exponent value measured in this study was 1.2, which agrees with the result of previous experiments (e.g., [4–6]). The power spectrum of the streamwise velocity fluctuations was also used for PIV validation. As shown in **Figure 4**, the power spectrum observed by our PIV technique agrees well with the laser-Doppler velocimetry measurements of our previous experiment [24], thereby indicating that the present PIV could accurately measure velocity fluctuations in grid-generated turbulence.

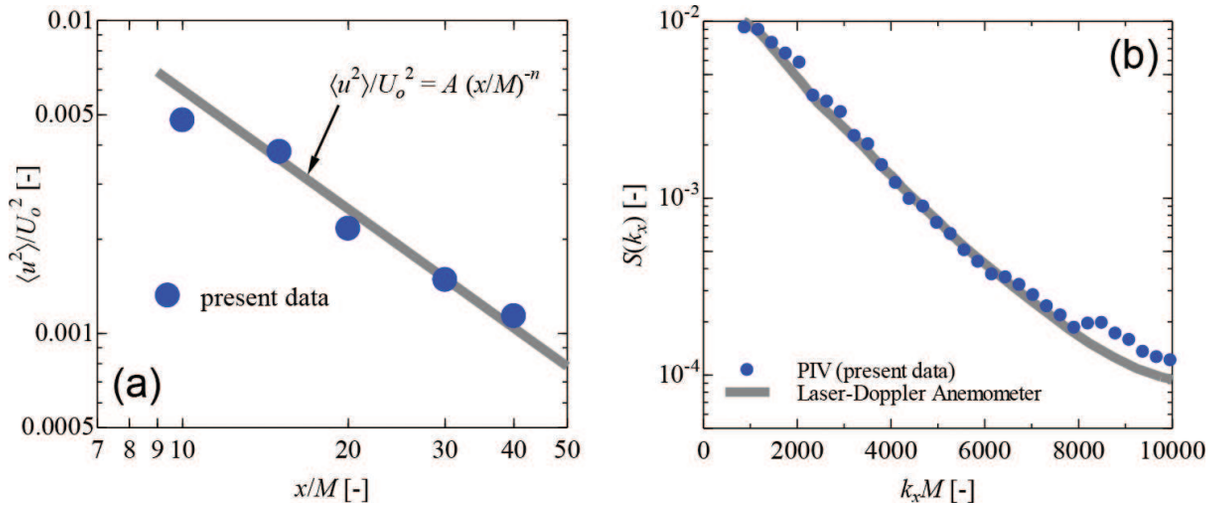

Figure 4. Validation of the present PIV measurement in grid-generated turbulence, where (a) and (b) show the normalized intensity of streamwise velocity fluctuation and power spectra of the streamwise velocity fluctuation at x/M = 18, where the laser-Doppler anemometer data are measured by Ito et al. (2002) [24]. The agreement shown here validates our current PIV measurements.

3. Results and discussion

3.1. Turbulent mixing and fractal dimensions

Here, we address the turbulent mixing of the high-Sc-number scalar in the grid-generated turbulence of SG2 and FG. **Figure 5(a)** and **(c)** shows the instantaneous scalar of the fractal grid turbulence and classical grid turbulence in which the instantaneous scalar is normalized by the initial scalar difference. As can be seen in the figure, the high-Sc-number scalar is mixed by the grid-generated turbulence. Furthermore, as also shown in the figure, the yellow region in the fractal grid turbulence is wider than that in the grid-generated turbulence. Note that the yellow color indicates a scalar value at the mixing interface, the normalized value of which is 0.5.

Figure 5(b) shows a transverse profile of the mean scalar at this streamwise distance. As can be seen in the figure, the magnitude of the transverse gradient at the centerline of the fractal grid turbulence is smaller than that in the grid-generated turbulence. **Figure 6(a)** and **(c)** shows instantaneous scalar fluctuations of the scalar-mixing layer around $x/M_{\mathrm{eff}} = 80$. As can be seen in the figure, similar to the instantaneous scalar results, the wider region in which the scalar fluctuation exists is also found in the case of the fractal grid turbulence. **Figure 6(b)** shows transverse profiles of the scalar fluctuation intensity. Here, it can be seen that the intensity profile width in the fractal grid turbulence is larger than that in the grid-generated turbulence.

Since enhancing scalar turbulent mixing increases the scalar-mixing layer width in grid-generated turbulence, the intensity of turbulent mixing is quantified by using a length scale that characterizes scalar-mixing layer width. **Figure 7** shows streamwise profiles of the mean scalar

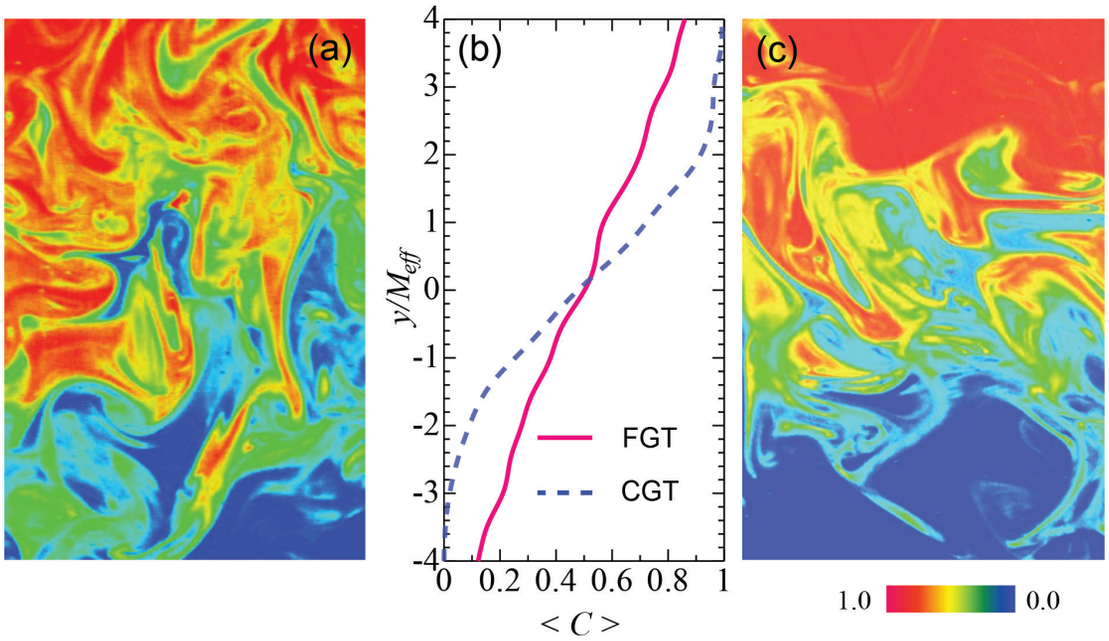

Figure 5. Instantaneous scalar field in the fractal-grid turbulence (FGT) (a) and conventional-grid turbulence (CGT) (c) around x/Meff = 80. The mean scalar profile at $x/M_{\mathrm{eff}} = 80$ is also shown in (b). Here red, yellow, and blue indicate C = 1, C = 0.5, and C = 0, respectively.

http://dx.doi.org/10.5772/67942

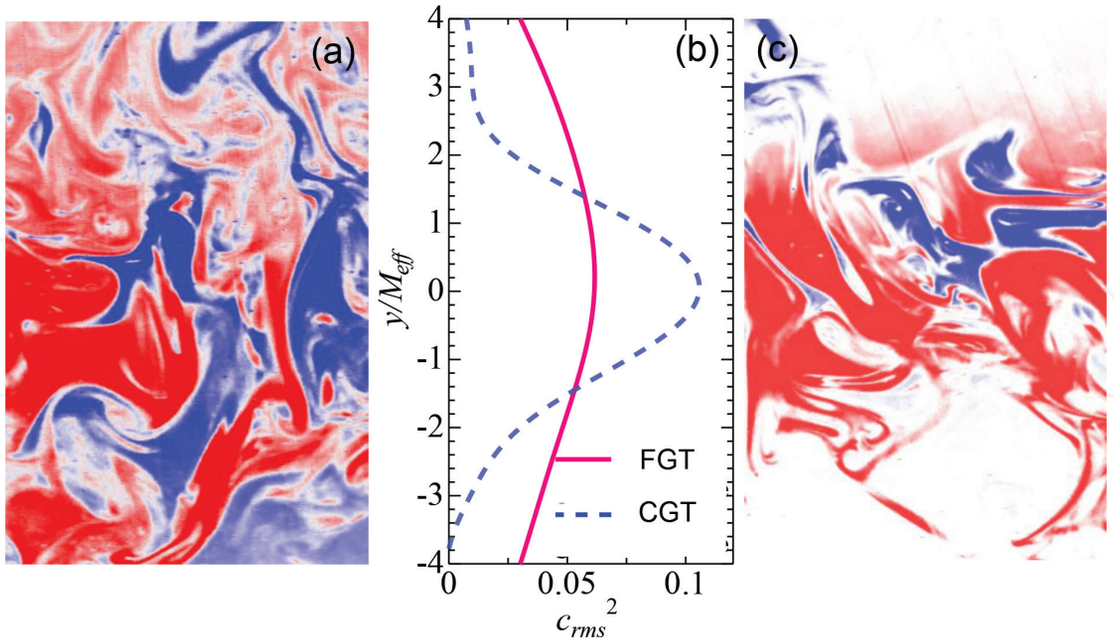

Figure 6. Instantaneous scalar fluctuation in the fractal-grid turbulence (FGT) (a) and conventional-grid turbulence (CGT) (c) around $x/M_{eff} = 80$. Scalar fluctuation intensity profiles at $x/M_{eff} = 80$ are also shown in (b).

profile half width. As can be seen in the figure, the mean scalar profile half widths in grid-generated turbulence follow a function of the square root of x/U, where x/U [s] is the time dimension and is referred to as convection time. In fractal grid turbulence, the half-width streamwise profile includes the mean scalar half-width profile, which is also characterized by the square root of x/U. Note that fractal grid turbulence half-width values are larger than those in grid-generated turbulence, thereby indicating that turbulent mixing is enhanced by using the fractal grid. The scalar fluctuation intensity width is also characterized by its half width. As with the mean scalar

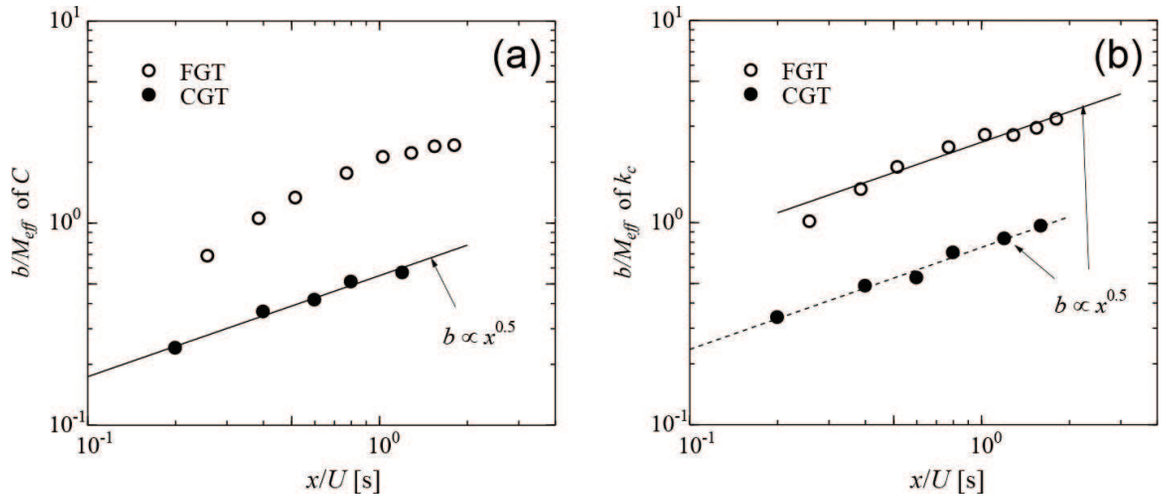

Figure 7. Profiles of the mean scalar half width and scalar variance as functions of the convection time x/U [s]. Here profiles of mean scalar half width and scalar variance half width are shown in (a) and (b), respectively. In the mean scalar and scalar variance results, the half width for the fractal-grid turbulence is larger than that for the conventional-grid turbulence.

half-width results, the larger half width of the scalar fluctuation intensity is found in the scalar-mixing layer due to fractal grid turbulence. These larger half-width values confirm the high-Sc-number scalar-mixing enhancement achieved by fractal grid application.

Next, we discuss the enhanced turbulent mixing of the high-Sc-number scalar in the fractal grid turbulence by calculating the fractal dimension using a box-counting method (e.g., [30, 31]). In the box-counting method, boxes that follow the relationship are counted: $|C - C_{th}| \approx 0$. Here, C and C_{th} are a value of the normalized scalar in the mixing layer and a threshold, respectively. The counted boxes satisfy the following relation: $N(\delta) = \alpha\ \delta^{-D}$, where δ is the characteristic length of the counted boxes and the area of the counted box is equal to δ^2.

Figure 8(a) shows a counted box value, which is a function of the scale δ, for the scalar-mixing layer in the fractal grid turbulence, where $x/M_{eff} = 40$ and $C_{th} = 0.5$. As shown in the figure, the counted box values decrease as the scale δ increases. Furthermore, the observed counted box value follows the basic relationship of the box-counting method, $N(\delta) = \alpha\ \delta^{-D}$. It should be noted that the value of D also depends on the scale δ, and that the scales δ in the large and small values of d show large- and small-scale scalar fractal dimension values. A value of D for the large δ, which is found to be constant, is different from that for the small δ. Here, the large- and small-scale fractal dimension values are within the range of 1–2.

A fractal dimension value, which is considered to differ between larger and smaller scales, is calculated for the fractal grid and classical grid turbulence. **Figure 8(b)** shows the observed values of the fractal dimension, where the convection time for the fractal grid turbulence is nearly equal to that for the classical grid turbulence. As the figure shows, scalar field fractal dimension values in fractal grid turbulence are larger than those found in the classical grid turbulence. These larger fractal dimension values are found in both large- and small-scale scalar fields. A large-scale fractal dimension value does not depend on the threshold value,

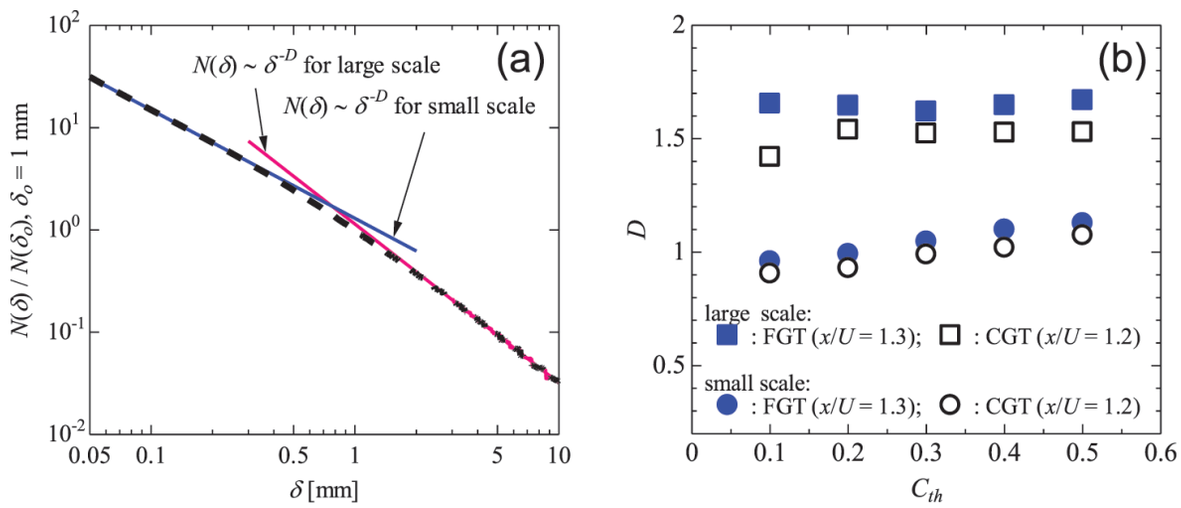

Figure 8. Counted boxes of the scalar field in the fractal-grid turbulence around $x/M_{eff} = 40$ and $C_{th} = 0.5$ (a), which are given by the box-counting method. Profiles of the counted boxes satisfy $N(\delta) \sim \delta^{-D}$. In (b), fractal dimension of the large- and small-scale scalar fields in fractal-grid and conventional-grid turbulence around $x/U = 1.25$ [s] are shown. The fractal dimension for the fractal-grid turbulence is larger than that for the conventional-grid turbulence.

http://dx.doi.org/10.5772/67942

although a small-scale fractal dimension value in the scalar field may depend slightly on the threshold value. The fractal dimension of a scalar field for which turbulent mixing does not occur is unity. Fractal dimension values approach two as turbulent mixing is enhanced because our PLIF measurement technique uses a two-dimensional measurement for the scalar field. The larger fractal dimension value found in turbulent mixing due to fractal grid turbulence indicates the enhancement of turbulent mixing achieved by using a fractal grid.

Figure 9 shows streamwise fractal dimension evolution as a function of convection time. Here, it can be seen that the fractal dimension of large-scale turbulent mixing resulting from fractal grid turbulence increases with convection time. The fractal dimension of the small-scale field for fractal grid turbulence is also larger than that for the classical grid turbulence, thereby indicating that fractal grid application could enhance both small- and large-scale turbulent mixing. Since the small-scale fractal dimension difference found between the two turbulence-generating grids would not be large, further experiments may be needed to determine the incremental fractal dimension increase achieved by applying the fractal grid.

3.2. Turbulent mixing device efficiency

Next, we discuss the enhancement of turbulent mixing achieved via fractal grid using PIV measurement results, starting by examining velocity fluctuation intensity. **Figure 10(a)** shows streamwise profiles of (3/2) $\langle u^2 \rangle$/(1/2) U_o^2, referred to hereafter as turbulence intensity. In the classical and fractal grid turbulence, the large-scale anisotropy is constant for time and approximates unity. Therefore, the quantity of the turbulence intensity (3/2) $\langle u^2 \rangle$/(1/2) U_o^2 would correspond to turbulent kinetic energy. The longitudinal direction is the convection time, which is normalized by the unit time [s].

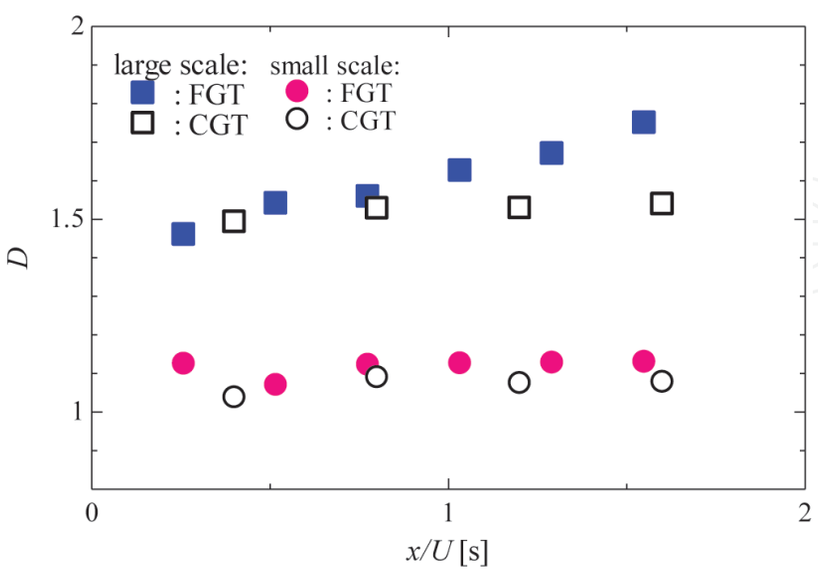

Figure 9. Streamwise profile of the fractal dimensions. The square and circle denote fractal dimension for large- and small-scale scalar fields, respectively. The fractal dimension for fractal-grid turbulence is larger than that for conventional-grid turbulence in large- and small-scale scalar fields.

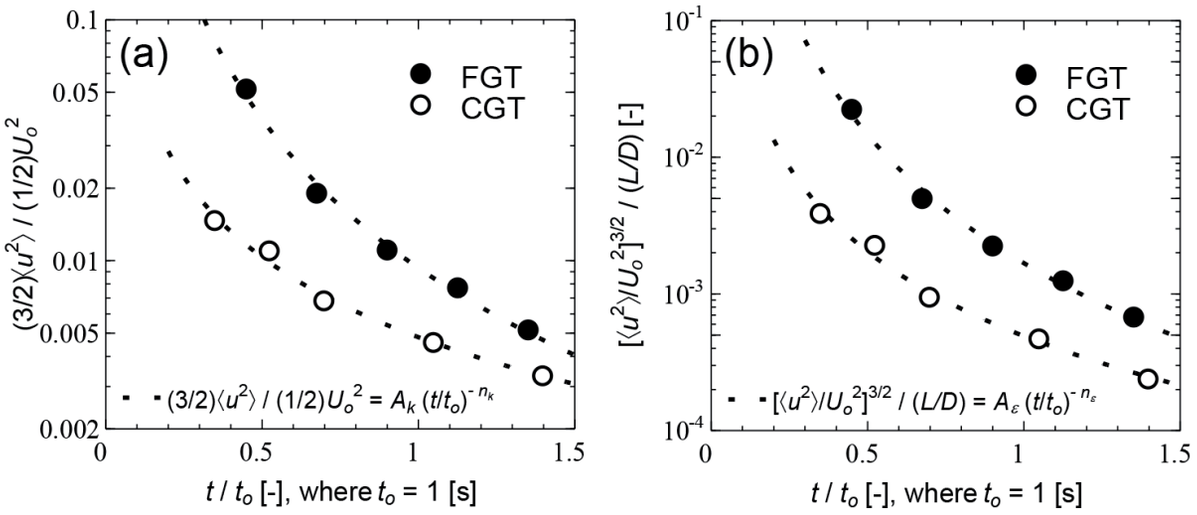

Figure 10. Streamwise profiles of the turbulent intensity (a) and the dissipation (b) for fractal-grid turbulence and conventional-grid turbulence, where the longitudinal direction is the normalized convection velocity. These profiles satisfy each power law with different decay exponent and decay coefficient values.

As shown in the figure, the classical and fractal grid turbulence intensities decrease as the convection time increases. Also, the fractal grid could be considered to generate decaying turbulence with a turbulence intensity that is larger in the same bulk energy magnitude because it is normalized by the bulk flow kinetic energy. The figure also shows that the classical grid turbulence intensity satisfies the following power law: $(3/2)\ \langle u^2\rangle/(1/2)\ U_o^{\ 2} = A_k\ (t/t_o)^{-nk}$, where A_k and n_k are the decay coefficient and decay exponent, respectively. Fractal grid turbulence intensity also follows a power law with the different parameter values.

Viscous dissipation is also examined in this study because the measurement allows potentially serious result uncertainties. Accordingly, observed viscous dissipation ε, which is referred to as dissipation, is calculated and defined as follows: $\varepsilon = [\langle u^2\rangle/U_o^{\ 2}]^{3/2}/(L/D)$. Here, L is the integral scale of the streamwise velocity fluctuation. As shown in **Figure 10(b)**, streamwise dissipation profiles in the classical and fractal grid turbulence also follow each power law: $[\langle u^2\rangle/U_o^{\ 2}]^{3/2}/(L/D) = A_\varepsilon\ (t/t_o)^{-n\varepsilon}$. Here, A_ε and n_ε are the decay coefficient and decay exponent of the dissipation, respectively.

Next, the decay exponents and decay coefficients of the fractal and classical grid turbulence are measured. **Figure 11(a)** shows the classical and fractal grid turbulence intensity decay exponents. As can be seen in the figure, the turbulence intensity decay exponents are measured as 2.1 for fractal grid turbulence and 1.1 for the classical grid, and the fractal grid turbulence decay exponent is larger than that for conventional grid turbulence. This larger fractal grid turbulence value implies that it includes dynamics other than the viscous dissipation, such as turbulent diffusion (e.g., [12]). **Figure 11(b)** shows the decay coefficients of fractal grid turbulence normalized by that of conventional grid turbulence, where the turbulence intensity decay coefficients and dissipation are shown.

As shown in the figure, the normalized decay coefficient value for fractal grid turbulence intensity is about two. Since a decay coefficient is directly related to the drag coefficient of a

http://dx.doi.org/10.5772/67942

turbulence-generating grid, a larger decay coefficient value for turbulence intensity would have a larger drag coefficient in the grid. Furthermore, since fractal grid turbulence size characteristics depend primarily on the largest and smallest grids, larger grids can be expected to produce larger grid drag coefficients. The dissipation decay coefficient of fractal grid turbulence normalized by the conventional grid turbulence is also shown in the figure, and is about 3.5. In turbulent diffusion, which is modeled by two-particle diffusion, the turbulent diffusion coefficient is proportional to viscous dissipation. Therefore, the decay coefficient increment of the dissipation indicates that of the turbulent diffusion coefficient. However, it should be noted that the dissipation decay coefficient increment is considerably larger than that of the turbulence intensity. Qualitatively, turbulent-mixing enhancement increases as the drag coefficient is increased. As can be seen in the figure, applying the fractal grid produces a drag coefficient-related dissipation increment that is related to turbulent diffusion coefficient and is larger than the turbulence intensity increment. Therefore, **Figure 11(b)** confirms the efficiency of a fractal grid as a device for enhancing turbulence mixing.

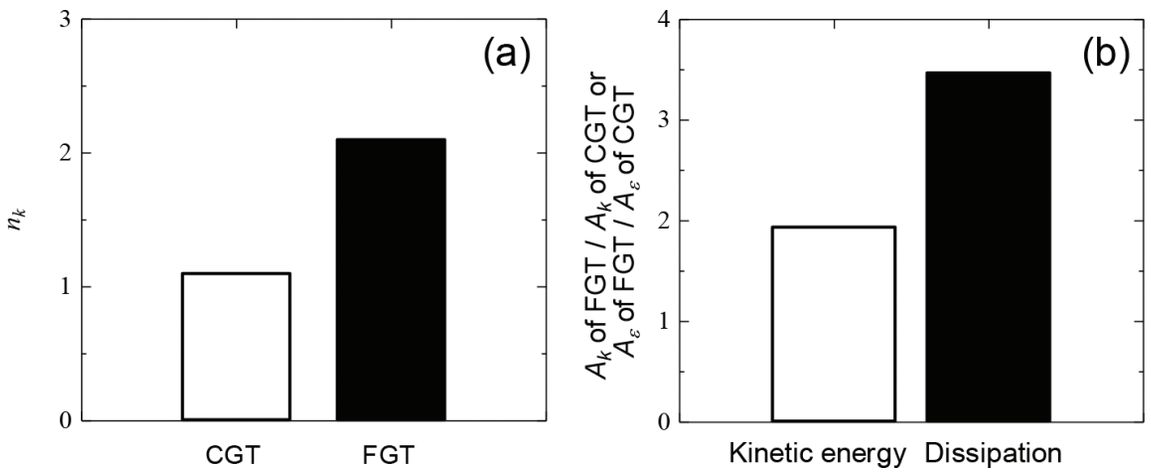

Figure 11. Decay exponents of the turbulent intensity (a) and the ratio of the decay coefficients between fractal-grid and conventional-grid turbulence (b). The dissipation decay coefficient increase, which relates to the turbulent diffusion coefficient, is larger than that of the turbulent intensity, which relates to the grid-drag coefficient.

4. Conclusion

This study has addressed high-Sc-number scalar turbulent mixing in decaying turbulence through experiments in which decaying turbulence was generated using a grid placed inside a uniform flow. In recent years, fractal grids, which are new turbulence-generating grids with shape-based fractal perspectives, have been proposed, and high-magnitude turbulent intensities have been found in the decaying turbulence produced by such grids. The present study applies the decaying turbulence produced by a fractal grid to high-Sc-number scalar turbulent mixing in a water channel experiment measured by PLIF and PIV in order to clarify fractal grid turbulence mixing. Conventional grid turbulence, which is produced via a biplane

conventional grid, was also measured. Fractal dimensions, which were calculated using the box-counting method as well as relevant statistics, were used to clarify high-Sc-number scalar turbulent mixing in the grid turbulences examined.

We started by validating the PLIF and PIV measurement techniques used and showed that our correction for laser attenuation effects caused by the dye used definitely improved scalar fluctuation measurement accuracy. Next, the PIV was validated by using the decay characteristics and spectra of conventional grid turbulence. As shown in the PLIF visualization results provided herein, the use of a fractal grid increased the scalar-mixing layer width, and the scalar-mixing layer width increment could be quantitatively observed by using the characteristics length of the mean scalar profile and scalar fluctuation intensity.

Our fractal dimension investigation, which was calculated in order to discuss high-Sc-number scalar turbulent mixing in fractal grid turbulence, showed that the use of a fractal grid could enhance both large- and small-scale turbulent mixing. The decay exponent, turbulence intensity decay coefficient, and dissipation were then calculated from PIV measurements, the results of which showed a larger decay exponent magnitude in fractal grid turbulence. Next, we discussed using the decay coefficient to quantify the efficiency of a fractal grid as a device for enhancing turbulent mixing. The results showed that when utilizing a fractal grid, the turbulent diffusion coefficient increase in the generated grid turbulence was found to be larger than the grid drag coefficient.

In our future works, the dynamics that are expected to be found in enhanced turbulent mixing due to fractal grid turbulence will be studied. By further investigating the phenomena from the perspective of dynamics, a new turbulent-mixing device may further be developed.

Acknowledgements

The authors gratefully acknowledge the assistance of Professor J. Christos Vassilicos of Imperial College London and Dr. Takashi Kubo of Meijo University, Nagoya, Japan. A portion of this study was carried out under the Research Cooperative Program between the Japan Society for the Promotion of Science and The Royal Society. This study was also supported in part by Grants-in-Aid (nos. 25289030, 25289031, and 15K17970) from the Japanese Ministry of Education, Culture, Sports, Science and Technology.

Author details

Hiroki Suzuki[1]*, Shinsuke Mochizuki[2], Yasuhiko Sakai[3] and Koji Nagata[3]

*Address all correspondence to: h.suzuki@yamaguchi-u.ac.jp

1 Graduate School of Sciences and Technology for Innovation, Yamaguchi University, Ube, Japan

2 Department of Mechanical Science and Engineering, Nagoya University, Nagoya, Japan

3 Department of Aerospace Engineering, Nagoya University, Nagoya, Japan

References

[1] Sreenivasan KR and Antonia RA: The phenomenology of small-scale turbulence. Annual Review of Fluid Mechanics. 1997;**29**:435–472. DOI: 10.1146/annurev.fluid.29.1.435

[2] Sreenivasan KR: Fractals and multifractals in fluid turbulence. Annual Review of Fluid Mechanics. 1991;**23**:539–604. DOI: 10.1146/annurev.fl.23.010191.002543

[3] Dimotakis PE: Turbulent mixing. Annual Review of Fluid Mechanics. 2005;**37**:329–356. DOI: 10.1146/annurev.fluid.36.050802.122015

[4] Comte-Bellot G and Corrsin S: The use of a contraction to improve the isotropy of grid-generated turbulence. Journal of Fluid Mechanics. 1966;**25**:657–682. DOI: https://doi.org/10.1017/S0022112066000338

[5] Mohamed MS and LaRue JC: The decay power law in grid-generated turbulence. Journal of Fluid Mechanics. 1990;**219**:195–214. DOI: https://doi.org/10.1017/S0022112090002919

[6] Suzuki H, Mochizuki S, and Hasegawa Y: Validation scheme for small effect of wind tunnel blockage on decaying grid-generated turbulence. Journal of Fluid Science and Technology. 2016;**11**:JFST0012. DOI: http://doi.org/10.1299/jfst.2016jfst0012

[7] Lavoie P, Djenidi L, and Antonia RA: Effects of initial conditions in decaying turbulence generated by passive grids. Journal of Fluid Mechanics. 2007;**585**:395–420. DOI: https://doi.org/10.1017/S0022112007006763

[8] Sinhuber M, Bodenschatz E, and Bewley GP: Decay of turbulence at high Reynolds numbers. Physical Review Letters. 2015;**114**:034501. DOI: https://doi.org/10.1103/PhysRevLett.114.034501

[9] Vassilicos JC: Dissipation in turbulent flows. Annual Review of Fluid Mechanics. 2015;**47**:95–114. DOI: 10.1146/annurev-fluid-010814-014637

[10] Hurst D. and Vassilicos JC: Scalings and decay of fractal-generated turbulence. Physics of Fluids. 2007;**19**:035103. DOI: http://dx.doi.org/10.1063/1.2676448

[11] Valente PC and Vassilicos JC: The decay of turbulence generated by a class of multi-scale grids. Journal of Fluid Mechanics. 2011;**687**:300–340. DOI: https://doi.org/10.1017/jfm.2011.353

[12] Nagata K, Sakai Y, Inaba T, Suzuki H, Terashima O, and Suzuki H: Turbulence structure and turbulence kinetic energy transport in multiscale/fractal-generated turbulence. Physics of Fluids. 2013;**25**:065102. DOI: http://dx.doi.org/10.1063/1.4811402

[13] Hearst RJ and Lavoie P: Decay of turbulence generated by a square-fractal-element grid. Journal of Fluid Mechanics. 2014;**741**:567–584. DOI: https://doi.org/10.1017/jfm.2013.684

[14] Nagata K, Saiki T, Sakai Y, Ito Y, and Iwano K: Effects of grid geometry on non-equilibrium dissipation in grid turbulence. Physics of Fluids. 2017;29:015102. DOI: http://dx.doi.org/10.1063/1.4973416

[15] Suzuki H, Nagata K, Sakai Y, and Ukai R: High-Schmidt-number scalar transfer in regular and fractal grid turbulence. Physica Scripta. 2010;**T142**:014069. DOI: http://dx.doi.org/10.1088/0031-8949/2010/T142/014069

[16] Gomes-Fernandes R, Ganapathisubramani B, and Vassilicos JC: Particle image velocimetry study of fractal-generated turbulence. Journal of Fluid Mechanics. 2012;**711**:306–336. DOI: https://doi.org/10.1017/jfm.2012.394

[17] Gomes-Fernandes R, Ganapathisubramani B, and Vassilicos JC: The energy cascade in near-field non-homogeneous non-isotropic turbulence. Journal of Fluid Mechanics. 2015;**771**: 676–705. DOI: https://doi.org/10.1017/jfm.2015.201

[18] Nagata K, Suzuki H, Sakai Y, Hayase T, and Kubo T: Direct numerical simulation of turbulent mixing in grid-generated turbulence. Physica Scripta. 2008;T132:014054. DOI: http://dx.doi.org/10.1088/0031-8949/2008/T132/014054

[19] Laizet S and Vassilicos JC: Multiscale generation of turbulence. Journal of Multiscale Modelling. 2009;**1**:177–196. DOI: http://dx.doi.org/10.1142/S1756973709000098

[20] Suzuki H, Nagata K, Sakai Y, and Hayase T: Direct numerical simulation of turbulent mixing in regular and fractal grid turbulence. Physica Scripta. 2010;**T142**:014065. DOI: http://dx.doi.org/10.1088/0031-8949/2010/T142/014065

[21] Laizet S and Vassilicos JC: DNS of fractal-generated turbulence. Flow, Turbulence and Combustion. 2011;**87**:673–705. DOI: 10.1007/s10494-011-9351-2

[22] Suzuki H, Nagata K, Sakai Y, Hayase T, Hasegawa Y, and Ushijima T: Direct numerical simulation of fractal-generated turbulence. Fluid Dynamics Research. 2013;**45**:061409. DOI: http://dx.doi.org/10.1088/0169-5983/45/6/061409

[23] Zhou Y, Nagata K, Sakai Y, Suzuki H, Ito Y, Terashima O, and Hayase T: Relevance of turbulence behind the single square grid to turbulence generated by regular- and multiscale-grids. Physics of Fluids. 2014;**26**:075105. DOI: http://dx.doi.org/10.1063/1.4890746

[24] Ito Y, Nagata K, and Komori S: The effects of high-frequency ultrasound on turbulent liquid mixing with a rapid chemical reaction. Physics of Fluids. 2002;**14**:4362–4371. DOI: http://dx.doi.org/10.1063/1.1518508

[25] Sponfeldner T, Soulopoulos N, Beyrau F, Hardalupas Y, Taylor AMKP, and Vassilicos JC: The structure of turbulent flames in fractal- and regular-grid-generated turbulence. Combustion and Flame. 2015;**162**:3379–3393. DOI: http://dx.doi.org/10.1016/j.combustflame.2015.06.004

[26] Sakai Y, Nagata K, Suzuki H, Ito Y: Mixing and diffusion in regular/fractal grid turbulence. In: Sakai Y, Vassilicos, JC, editors. Fractal Flow Design: How to Design Bespoke Turbulence and Why: Springer International Publishing; 2016. pp. 17–73. DOI: 10.1007/978-3-319-33310-6

[27] Crimaldi JP: Planar laser induced fluorescence in aqueous flows. Experiments in Fluids. 2009;**44**:851–863. DOI: 10.1007/s00348-008-0496-2

[28] Suzuki H, Nagata K, and Sakai Y: Quantitative visualization of high-Schmidt-number turbulent mixing in grid turbulence by means of PLIF. Journal of Visualization. 2012;**15**:109–117. DOI: 10.1007/s12650-011-0121-y

[29] Raffel M, Willert CE, Wereley S, and Kompenhans J: Particle Image Velocimetry: A Practical Guide. Springer-Verlag Berlin Heidelberg; 2013. DOI: 10.1007/978-3-540-72308-0

[30] Villermaux E and Innocenti C: On the geometry of turbulent mixing. Journal of Fluid Mechanics. 1999;**393**:123–147. DOI: https://doi.org/10.1017/S0022112099005674

[31] Suzuki H, Nagata K, Sakai Y, and Hasegawa Y: Fractal analysis of turbulent mixing in fractal-generated turbulence by planar laser-induced fluorescence. Physica Scripta. 2015;**T155**:014062. DOI: http://dx.doi.org/10.1088/0031-8949/2013/T155/014062

IntechOpen